JACS
JOURNAL OF THE AMERICAN CHEMICAL SOCIETY

Nanofluid-Assisted Synthesis of High-Entropy Alloy Nanoparticles

Di Yin, Liqiang Wang, You Meng, Mengxue Chen, Dong Chen, Chenxu Zhang, Quan Quan, Haifan Li, Liyuan Dai, Lijie Chen, Cheng Yang, SenPo Yip,* Chun-Yuen Wong, Takeshi Yanagida, Yang Lu,* and Johnny C. Ho*

Cite This: https://doi.org/10.1021/jacs.5c22716 Read Online

ABSTRACT: The synthesis of high-entropy alloy nanoparticles (HEA-NPs) has traditionally been guided by thermodynamic considerations, relying on static parameter optimization. Here, we introduce a kinetically controlled paradigm for directing nanofluid transport to craft strained HEA-NPs from ten dissimilar elements. This strategy employs Zn as an active propellant, constructing interconnected nanochannels that steer multimetal nanofluid flow and trigger alloying. Using in situ transmission electron microscopy, we directly observe the dynamics of long-range directional migration under nanoconfinement, which induces forced fusion and fission events pivotal for achieving homogeneous mixing and size control. These unique confinement dynamics further impart surface tensile strain to the resulting nanoparticles. When applied to electrocatalytic nitrate-to-ammonia conversion, the strained HEA-NPs achieve an exceptional Faradaic efficiency of 94.8 ± 4.34% and sustain stable operation for over 720 h. Mechanistic studies attribute this performance to the synergy between multielement active sites and the tailored surface strain, which collectively optimize intermediate adsorption. This work establishes a new design principle for complex nanomaterials by shifting the perspective from static thermodynamics to dynamic kinetic control, providing a scalable pathway for the development of advanced electrocatalysts.

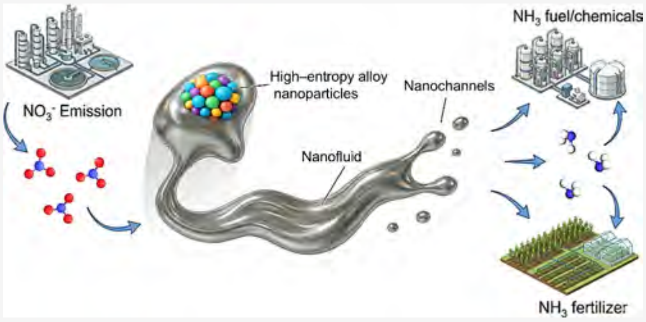

1. INTRODUCTION

High-entropy alloy nanoparticles (HEA-NPs) have attracted significant interest in various emerging energy-related applications, with a pronounced role in catalysis.[1−3] In particular, multielement alloying, a method capable of fabricating individual nanoscale products, can provide more active site exposure and allow for customizable compositional variations in catalyst design.[4,5] However, the vastly different chemical and physical properties of the constituent elements result in a wide range of mixing enthalpies, posing significant challenges for achieving spontaneous thermodynamic alloying.[6,7] Interestingly, Ga, which possesses a negative mixing enthalpy with other metals, could serve as an ideal reservoir, ensuring a stable thermodynamic condition.[8] Unfortunately, only a limited number of element systems can realize such thermodynamically favorable alloying. Therefore, in addition to thermodynamic tuning, it is crucial to conduct comprehensive investigations into the synthesis of HEA-NPs.

The successful synthesis of HEA-NPs heavily depends on the kinetic control of the alloying process, as dynamic fusion behaviors promote elemental mixing.[6,9] The liquid state of multiple elements typically facilitates atom diffusion due to weakened metallic bonds. However, achieving homogeneous alloying among multiple immiscible elements is challenging. Overcoming immiscibility gaps to form a uniform solid solution often necessitates high temperatures to drive entropy-stabilized mixing.[9−11] Moreover, while the melting point of metal nanoparticles decreases with size, short heating durations followed by rapid quenching remain essential to maintain small particle size and the single-phase mixing state of HEA-NPs, generally necessitating specialized synthetic techniques.[12−15] Nanofluids exhibit potential as an optimal liquid alloying environment for achieving homogeneous high-entropy mixing at low temperatures.[16] This dynamic reaction matrix could enhance synthetic kinetics and confine HEA formation to the nanoscale.[8,17] Surprisingly, this dynamic alloying strategy remains largely unexplored, primarily due to the daunting tasks associated with its implementation and the need for an in-depth understanding of this nanoreactor. In this regard, the development of a nanofluid-assisted dynamic manufacturing strategy is of significant importance, offering

Received: December 18, 2025
Revised: April 7, 2026
Accepted: April 13, 2026

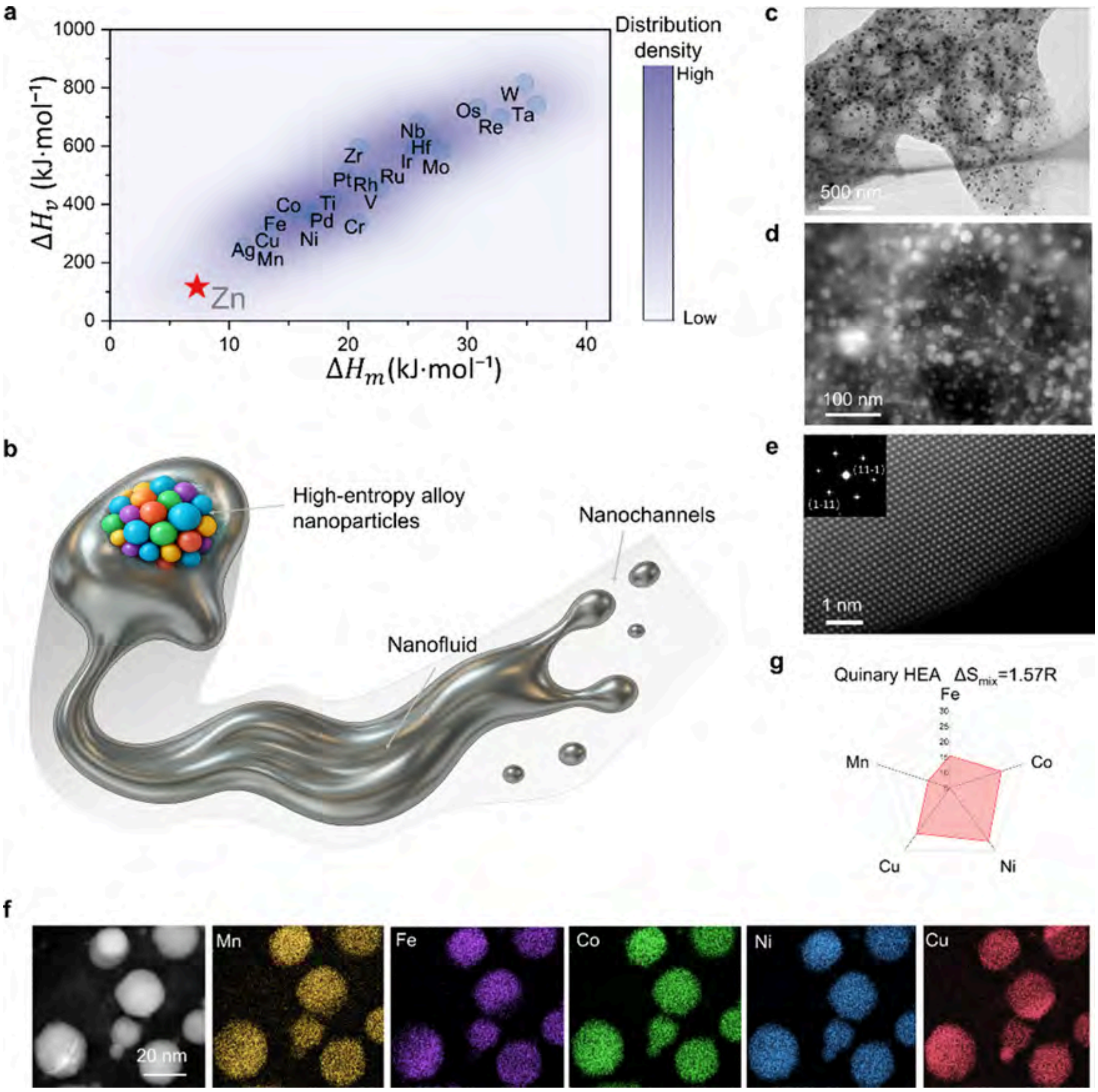

Figure 1. Synthesis of the HEA-NPs anchored on the porous carbon framework. (a) Selecting metals based on the enthalpy of fusion (ΔH_m)/vaporization (ΔH_v). (b) Schematic diagram of the nanofluid-assisted dynamic alloying strategy for the HEA-NP synthesis. (c) and (d) TEM image of HEA-NPs on a 3D carbon network. (e) Aberration-corrected HAADF-STEM of the MnFeCoNiCu HEA-NP. The inset image shows the SAED image of the MnFeCoNiCu HEA-NP. (f) STEM accompanied by elemental maps of the MnFeCoNiCu HEA@C. (g) Atomic percentages of metals in the MnFeCoNiCu HEA@C as determined by ICP-OES.

broader approaches to achieve robust high-entropy mixing under mild conditions.

In this work, we present a kinetically controlled method that uses zinc as an active sacrificial element to construct interconnected nanochannels. These nanochannels guide the flow of a multimetal nanofluid, thereby initiating the alloying process and enabling the synthesis of strained HEA-NPs from ten distinct elements. Furthermore, by employing in situ transmission electron microscopy (TEM)-based heating, we directly observe that nanofluids undergo directional motion over extended distances within these nanochannels, a dynamic process that triggers forced fusion and enhanced diffusion, thereby achieving homogeneous mixing. The unique nanoconfinement dynamics during synthesis endow the resulting HEA-NPs with significant surface tensile strain. When evaluated as catalysts for the nitrate reduction to ammonia reaction, our strained quinary HEA-NPs achieve a Faradaic efficiency of 94.8 ± 4.34% and maintain remarkable stability over 720 h. Mechanistic studies indicate that the enhanced catalytic performance arises from the synergy of multiple active sites and the introduced surface strain, which collectively optimize the adsorption energy of key reaction intermediates.

2. RESULTS

2.1. Active-Sacrificial Strategy for HEA-NP Synthesis

We selected a Zn-based MET-6 framework as the precursor, and preloaded it with multiple metal ions (Mn, Fe, Co, Ni, Cu). The detailed preparation process and related characterizations are described in the Methods section and Note S1 (Figures S1−S5 and Table S1). The synthesis of HEA-NPs is facilitated by the strategic incorporation of zinc, which leverages its low melting enthalpy (ΔH_m) and vaporization enthalpy (ΔH_v). As illustrated in Figure 1a, zinc's low ΔH_v enables it to melt and volatilize during pyrolysis, acting as a sacrificial template. This process generates a substantial vapor flux within the MOF-derived carbon matrix, thereby creating interconnected nanochannels. Within this confined architec-

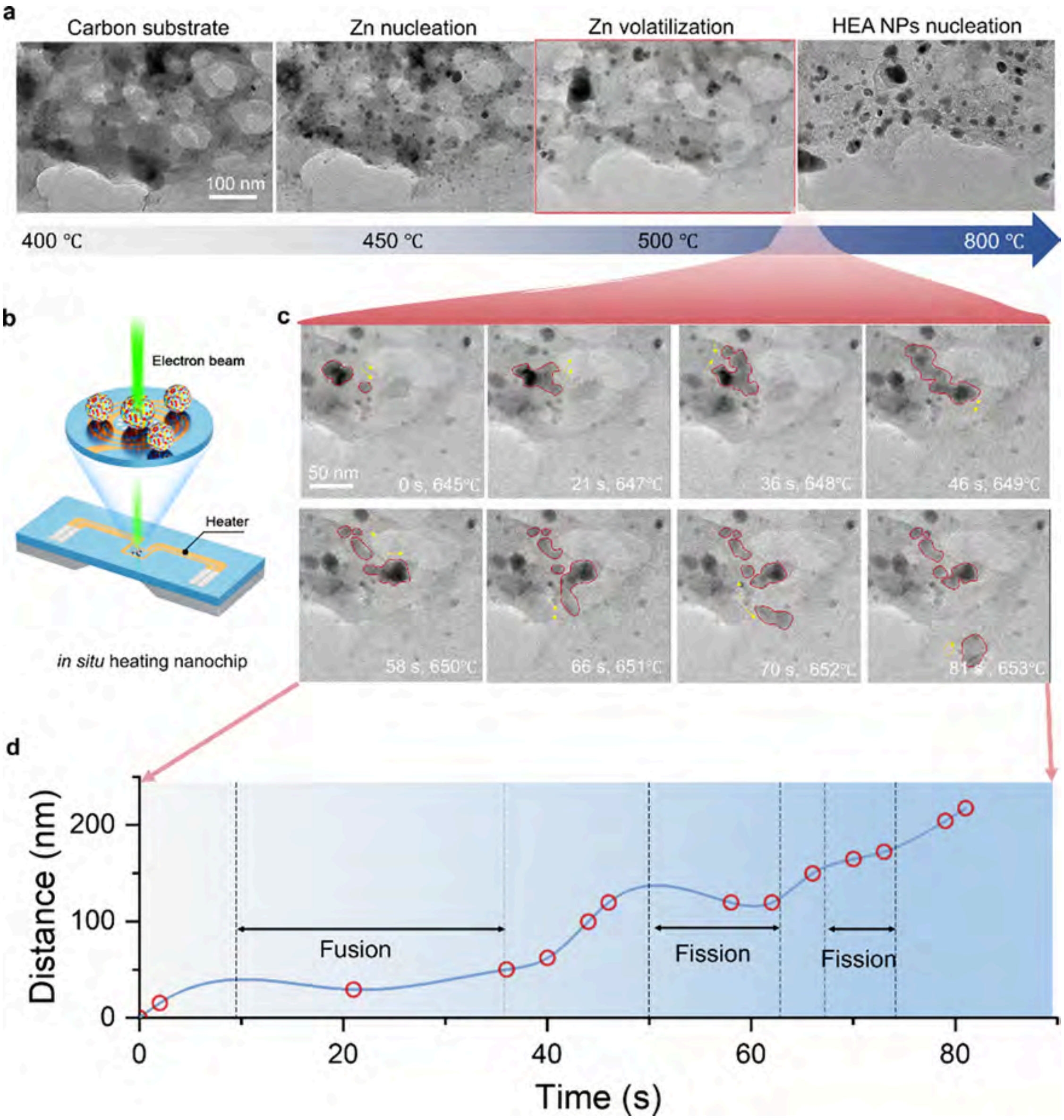

Figure 2. In situ TEM visualization of nanofluid-assisted HEA-NP synthesis. (a) In situ TEM observation of the formation of HEA-NPs on carbon support. (b) Schematic image of in situ TEM observation. Resistance wires on the nanochip allow for accurate temperature regulation. (c) In situ TEM observation of nanofluid migration on amorphous carbon support. Sequential images were captured during a time series from 0 to 81 s. The scale bars are 50 nm. (d) The migration distance of nanofluids versus time during a representative fusion-fission process, where the coalescence and fission events are highlighted, respectively.

ture, the preloaded metallic elements are steered to flow and alloy into single-phase HEA-NPs (Figure 1b; see Note S2 and Figure S6 for the detailed mechanism of cascade thermal activation and alloying).

After one-step pyrolysis at 800 °C, TEM imaging reveals that the porous carbon framework contains interconnected nanochannels, which uniformly anchor well-crystallized MnFeCoNiCu HEA-NPs (Figure 1c−e). Furthermore, TEM equipped with energy-dispersive spectroscopy (TEM-EDS), X-ray photoelectron spectroscopy (XPS), and inductively coupled plasma-optical emission spectrometry (ICP-OES) results confirmed that the low-boiling-point Zn composition was volatilized. The compositional ratios of other metals exhibited slight deviations from the starting ratio of the transition-metal-doped MOF precursor (Figure S7 and Table S2). According to the elemental compositions of MnFeCoNiCu, their configurational entropy (ΔS_{mix}) exceeded 1.5R, classifying them as HEA materials (Table S3).[18] TEM-EDS from nano to atomic scale confirms the homogeneous elemental distribution (Mn, Fe, Co, Ni, Cu) without segregation, and verifies their atomic-level mixing as a random solid-solution within the FCC lattice (Figures 1f and S8). Macroscopically, X-ray Diffraction (XRD) analysis confirms the formation of a solid solution without phase separation (Figure S9).[19] XPS results showed that each element in HEA-NPs mostly exists in the metallic state (Figure S10).[20] Figure S11 presents the high-resolution XPS spectra at four distinct etching depths (0, 1, 2, and 3 nm). The quantitative analysis reveals that the relative atomic ratios of the constituent elements remain highly consistent across the sequential etching stages. The absence of significant elemental segregation,

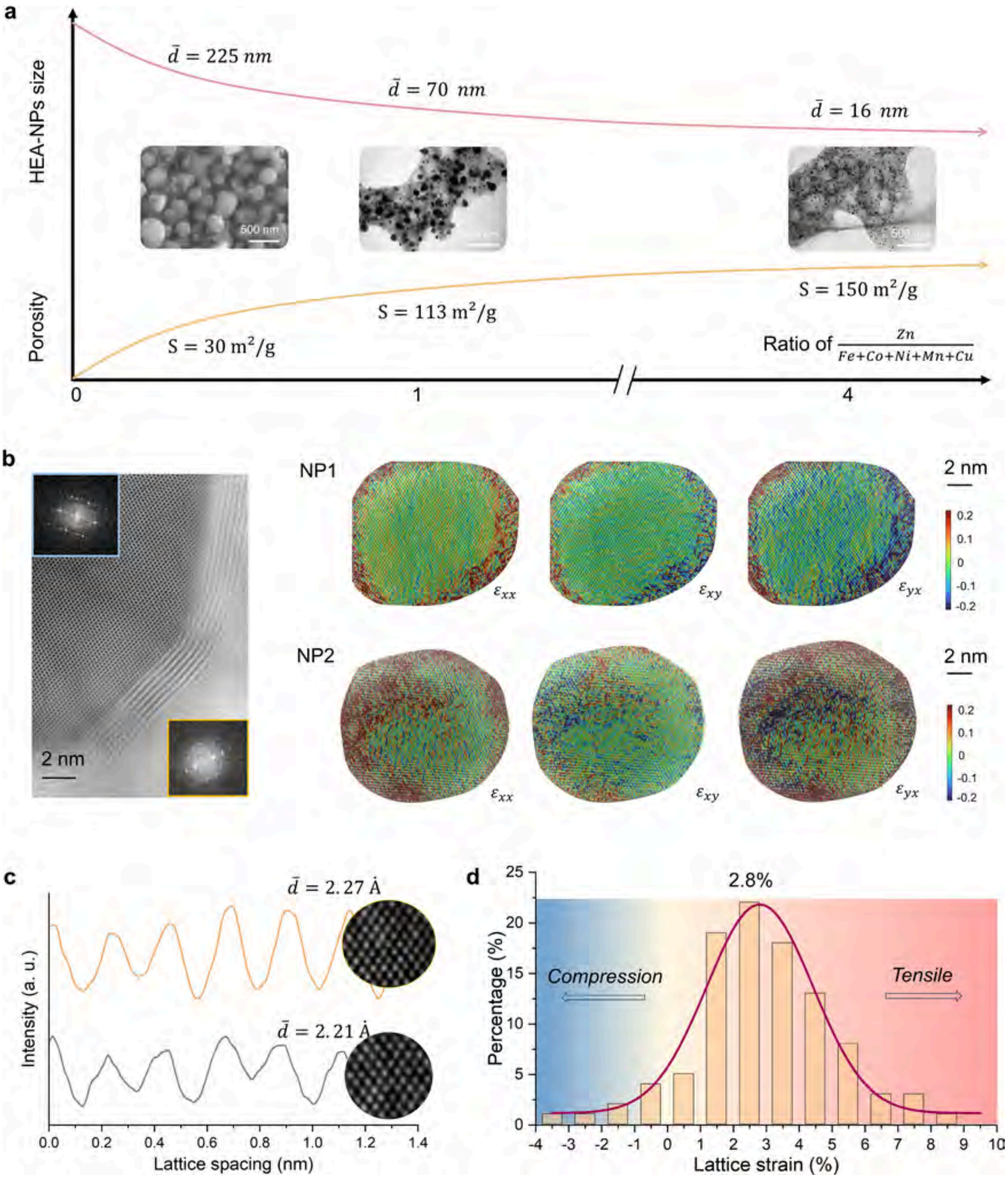

Figure 3. Nanoconfinement effect in synthetic HEA-NPs. (a) Effect of Zn content on HEA-NP size and carbon substrate porosity. (b) Aberration-corrected HAADF-STEM of a MnFeCoNiCu HEA-NP confined by the graphitized carbon, and the GPA patterns of typical HEA-NPs, with each small graph representing the atomic strain distribution in the ε_{xx}, ε_{xy}, and ε_{yy}. The inset image shows the SAED image of the MnFeCoNiCu HEA-NP and the graphitized carbon shell. (c) HRTEM measurement of the local lattice strain at the surface and interior regions of NP1. (d) Statistical distribution of the NP surface tensile strain.

specific elemental depletion, or enrichment at the outermost layer confirms the compositional uniformity of the HEA-NPs.

In this study, Zn was employed as an active sacrificial element to mediate the synthesis of HEA-NPs under mild conditions, thereby mitigating the reliance on conventional extreme temperatures or rapid cooling rates. More importantly, our synthesis strategy for HEA nanoparticles demonstrates wide applicability, enabling the synthesis of complex multi-component alloy nanoparticles containing up to 14 dissimilar elements. To rigorously verify the phase purity of these highly complex systems, specifically the 5-element FeCoNiCuCr, 6-element FeCuCoNiPdRu, 7-element CoFeAgAlPdCaRh, and 10-element CoCuFeNiMnMoPdPtRuSn, comprehensive structural and compositional analyses were conducted. The XRD patterns for all samples exhibit sharp peaks consistent with a single-phase solid solution, indicating no obvious phase separation. This macroscopic structural integrity is strongly corroborated by quantitative ICP-OES analyses confirming their near-equimolar stoichiometries, as well as HAADF-STEM combined with corresponding EDS mapping, which confirms the uniform distribution of all constituent elements within individual nanoparticles (Figures 1g, S12−S15, and Tables S4−S8). Collectively, these characterizations prove the successful synthesis of genuine, unsegregated high-entropy alloys across diverse multimetallic systems. These alloying elements have a range of preferred crystal structures (body-centered cubic, face-centered cubic, or hexagonal close-packed), melting temperatures (232−2623 °C), and atomic radii (1.24−1.97 Å).

2.2. In Situ TEM Visualization of Nanofluid-Assisted Synthesis of HEA Nanoparticles

To elucidate the role of Zn and the underlying synthesis mechanisms, an in situ TEM Joule-heating experiment is performed using a MEMS-based heating holder. The MET-6 precursor dispersion was drop-casted onto a silicon nitride membrane supported by a silicon nanochip.[21,22] The morphological changes in the precursors are visualized in a series of bright-field TEM images (Figure 2a,b). Initially, at temperatures below 400 °C, the precursor metal-triazole-metal linkages decomposed and expanded, forming a micrometer-scale porous carbon framework with limited nucleation of metallic nanoparticles (Figure S16).[23] Above 400 °C, Zn nanoparticles nucleated uniformly and then volatilized, creating internal cavities and interconnected channels (Figure 2a and Movie S1). To verify this sequential nucleation step compositionally, an ex situ control experiment was conducted by rapidly quenching the intermediate sample at 450 °C. Subsequent high-resolution elemental mapping confirmed that these initially formed nanoparticles are predominantly composed of Zn, whereas the other principal transition metals remain homogeneously dispersed within the surrounding carbon matrix (Figure S17). This active-sacrificial process yielded an interconnected nanoporous architecture designed to confine nanofluids afterward.

Upon further increasing the temperature, it exceeds the thermal decomposition temperature of the metal precursors, and many transition-metal salts begin to decompose, entering the liquid phase. Surprisingly, widespread and rapid nanofluidic flow events propagate through newly formed internal nanochannels (Movie S2). A representative process is depicted in Figure 2c. For detailed analysis, the onset of nanofluid flow was designated as time zero. Within the first 36 s, the nanofluid's motion enables dispersed NPs to encounter and coalesce continuously. This is followed by fission events occurring between 50−63 s and 68−74 s, during which a narrow channel forms during droplet migration and subsequently splits into distinct regions (Figure 2d). Statistical analysis of nanoparticle motion trajectories from in situ videos revealed a wave-like pattern in displacement over time, with a calculated average nanofluid velocity of 5.5 nm/s (Figure S18). The observed fusion-fission events can be attributed to the competition between the surface tension of the carbon substrate and the gas emission.[9] The dynamic motion of the nanofluid may be intimately linked to localized gas emission. However, to accurately interpret this driving force, it is necessary to distinguish the gas generation into two distinct stages as confirmed by online thermogravimetric analysis with mass spectrometry (TGA-MS) (Figure S19). The initial release of CO_2 and N_2 (300−400 °C) originates from the thermal decomposition of the precursor's metal-triazole-metal linkages. Subsequently, in the higher-temperature window (600−800 °C), where the multimetallic components transition into a nanofluid, a secondary generation of CO_2 occurs due to high-temperature carbon reconstruction and interfacial carbothermal reactions. It is this specific high-temperature CO_2 emission that acts as the powerful active propellant for the dynamic motion of the nanofluids.[24] However, variations in the surface tension of the carbon substrate occasionally hinder nanofluid transport, leading to repeated fusion-fission events of NPs during the alloying process.[8] This unique behavior of nanofluids can effectively enhance elemental mixing of high-entropy alloy nanoparticles.

2.3. Nanoconfinement Effect in HEA-NP Synthesis

The flow of metallic nanofluids within interconnected nanochannels provides a unique microenvironment for synthesizing HEA-NPs.[25] To elucidate the specific role of the active-sacrificial Zn, we fabricated three precursor samples, denoted as R0, R1, and R4, where "R" represents the initial molar ratio of Zn to the total five principal elements (Fe, Co, Ni, Mn, and Cu) at 0, 1, and 4, respectively. In all cases, the amounts of the five principal elements were kept constant to ensure comparability. The detailed step-by-step synthetic procedures are provided in the Supporting Information (Methods). Brunauer−Emmett−Teller (BET) analysis revealed that a higher content of Zn significantly enhanced evaporation kinetics during the heating process, leading to a substantial increase in porosity, as reflected by the rise in specific surface area from 30 to 150 $m^2 \cdot g^{-1}$ (Figures 3a and S20a).[26] Moreover, the incorporation of Zn resulted in a highly nanoporous architecture, as evidenced by the abundance of nanopores predominantly sized between 20 and 30 nm (Figure S20b). These nanochannels promoted fluid dynamics within the metallic nanoflow, thereby intensifying the chaotic nucleation and growth of HEA-NPs.[27] As a result, the HEA-NP diameter was effectively reduced from 225 nm (R0) to 16 nm when the Zn content was quadrupled relative to the other metallic elements (R4) (Figures 3a and S21). In addition, XRD analysis confirmed that the R4 sample formed a solid solution. In contrast, the R0 and R1 samples exhibited an undesirable phase separation (Figure S22). Fick's first law suggests an exponential relationship between ion-diffusion flux and synthesis temperature, where the increase in synthesis temperature leads to a sudden rise in the ion-diffusion capacity.[28,29] Therefore, conventional HEA-NP synthesis typically relies on extremely high temperatures to enhance the diffusion behavior of various metal/alloy nanoparticles.[30] In our study, the interconnected nanochannels provide spatial confinement during the nanofluid-assisted alloying process, significantly reducing atomic diffusion distances and restricting nucleation size. This configuration also enhances the stochastic motion of metal atoms within the nanofluid. Through repeated collisions, potential energy is converted into thermal energy, which locally raises the temperature and facilitates alloying.[31] In this manner, the nanofluid system promotes the fusion-fission events of immiscible nanoparticles under dynamic conditions, creating an ideal environment for the formation of small, single-phase HEA-NPs.

On the other hand, fusion-fission events in nanofluids confined in nanostructures revealed a strong interaction between nanoparticles and the carbon substrate. When the carbon layer fully encapsulates the nanoparticle, the carbon shell closely conforms to the surface of the HEA crystalline core at the atomic scale, thereby forming an incoherent interface (Figure 3b).[32,33] To maintain lattice matching with the tube wall or to reduce interfacial energy, HEA-NPs generate mismatch strain at the interface. We employ geometric phase analysis (GPA) to conduct strain analysis of typical MnFeCoNiCu HEA-NPs. The derived strain maps

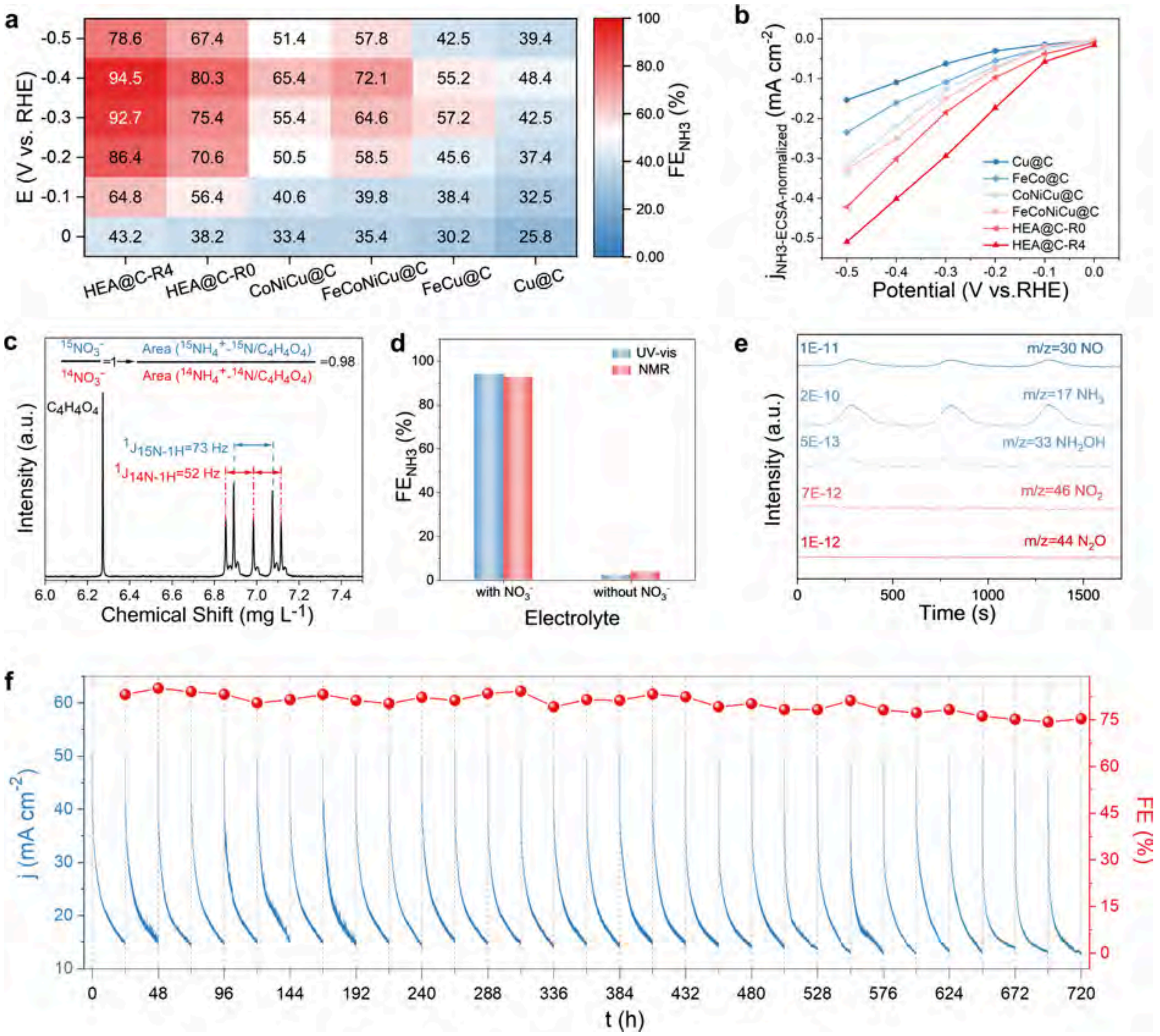

Figure 4. Electrocatalytic NO_3^--to-NH_3 conversion. (a) NH_3 Faradaic efficiency of the Cu@C, FeCu@C, CoNiCu@C, FeCoNiCu@C, HEA@C-R0, and HEA@C-R4 in a 0.5 M Na_2SO_4 electrolyte with 0.1 M NO_3^-. (b) ECSA normalized partial current densities in LSV curves of Cu@C, FeCu@C, CoNiCu@C, FeCoNiCu@C, HEA@C-R0, and HEA@C-R4 in an electrolyte of 0.5 M Na_2SO_4 and 0.1 M $NaNO_3$. (c) The ^1H NMR spectra of the electrolyte after NO_3RR with $^{14}NO_3^-$ /$^{15}NO_3^-$ in a ratio of 1 to 1 as feed. (d) The quantitative comparison of Faradaic efficiency over HEA@C based on the ^1H NMR and UV−vis method in a 0.5 M Na_2SO_4 electrolyte with and without NO_3^-. (e) In situ DEMS measurements of NO_3RR over HEA@C at −0.4 V versus RHE in NO_3^--contained solution. (f) Chronoamperometric profiles and Faradaic efficiency of the HEA@C-R4 during 30 repeated electrolysis tests (each test lasting 24 h).

exhibit a similar trend, where the grain interiors remain relatively strain-free, while significant lattice strain is localized near the NP surfaces.[34,35] This spatial gradient unequivocally confirms that the 2.8% net tensile strain is an extrinsic geometric feature driven by the strong interfacial interactions in the nanoconfinement, acting synergistically with the intrinsic atomic-level distortions. To quantify the surface strain effect, the matrix lattice spacing in the surface and interior regions of NP1 was compared using HRTEM images. The measured (111) lattice spacing was 2.21 Å in the interior, and 2.27 Å at the surface, corresponding to a localized tensile strain of approximately 2.7% (Figure 3c). Projected strain measurements for many nanoparticles are quantitatively summarized in the histograms presented in Figure 3d. These data collectively demonstrate an average tensile strain of 2.8% within the surface regions of these NPs. Detailed Rietveld refinements of the corresponding XRD indicate slight shifts in the FCC diffraction peaks of the MnFeCoNiCu HEA, confirming the existence of lattice distortions in HEA-NPs (Figure S23).

2.4. Application of HEA-NPs in Electrocatalytic NO_3RR

HEA-NPs with multielemental synergy and surface tensile strain demonstrate exceptional electrocatalytic potential.[36,37] We studied their performance for nitrate-to-ammonia conversion, where they demonstrated high activity and stability. Benefiting from the highly porous and interconnected 3D nanochannel network carved by the Zn propellant, both the externally dispersed and internally embedded HEA nanoparticles remain fully accessible to the bulk electrolyte, acting synergistically as highly effective active sites for NO_3RR. The electrocatalytic nitrate reduction performance was initially assessed using linear sweep voltammetry (LSV) in 0.5 M Na_2SO_4 with and without 0.1 M $NaNO_3$ (Figure S24a). The current density increases sharply with NO_3^- addition over a broad range of negative potentials from −0.1 to −0.5 V. At the

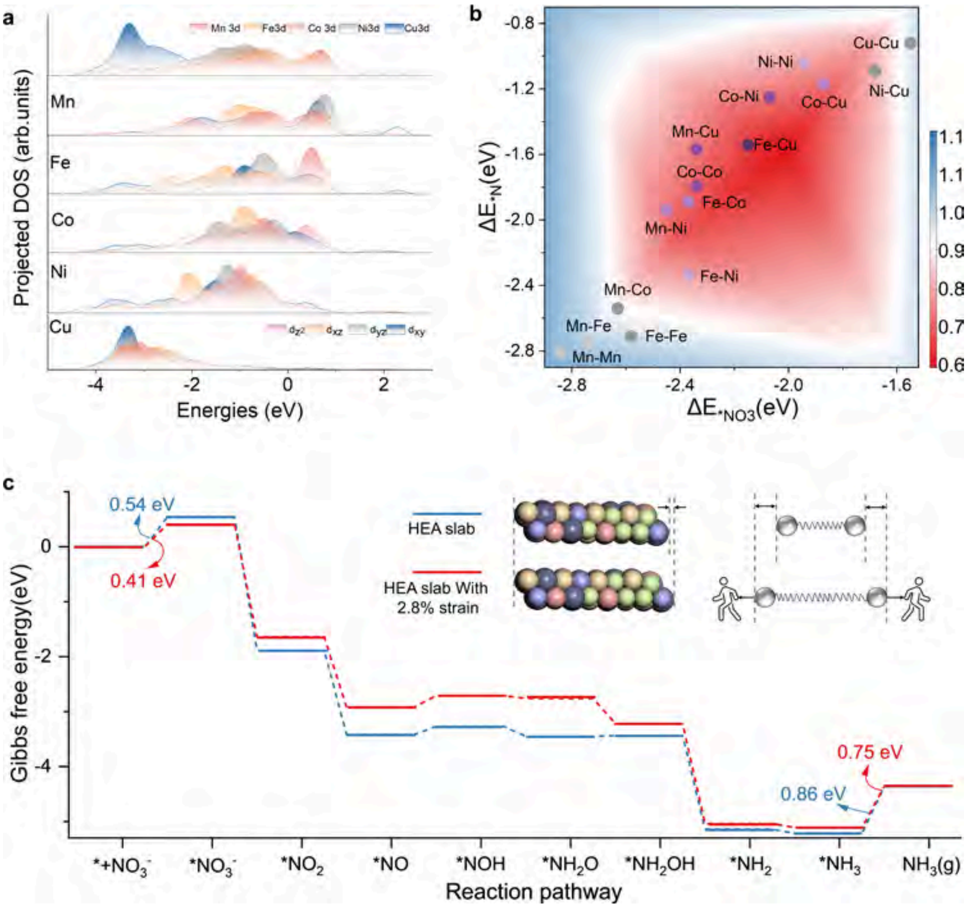

Figure 5. Theoretical analyses of the catalytic mechanism. (a) The projected electronic density of states for the d orbital of different metals in HEA with a 2.8% strain model. (b) Study the activity of various active sites in the strained HEA model using the activity volcano plot of NO_3RR to NH_3. (c) Free-energy diagram for NO_3RR on HEA and on HEA with the 2.8% strain.

same time, it delivers a nearly zero current density during this potential range in a pure Na_2SO_4 solution. At < −0.5 V, the current density increased dramatically due to intense competition from the H_2 evolution reaction (HER). The lower overpotentials for NO_3RR facilitate high selectivity for the NO_3^--to-NH_3 conversion.[38] To verify the multielemental synergy and intrinsic tensile strain advantages of HEA@C, the electrochemical properties of the HEA@C-R4, HEA@C-R0, Cu@C, FeCu@C, CoNiCu@C, and FeCoNiCu@C catalysts were compared under the same conditions. LSV was first conducted to compare the activity of the as-synthesized HEA@C-R4 with that of other comparison catalysts (Figure S24b). The obtained curves show HEA@C-R4 has the lowest onset potential and the highest increase of current density in a wide range from −0.1 V to −0.5 V. To confirm the LSV analytic results, we further quantified the NH_3 Faradaic efficiency (FE_{NH3}) and the yield rate of NH_3 (Y_{NH3}) in controlled-potential electrolysis (Figures 4a, S25, and S26). As the electrode potential shifted negatively, the FE_{NH3} initially increased and then decreased from −0.4 V to −0.5 V. As expected, the HEA@C-R4 catalyst achieved the highest Y_{NH3} of 11.3 ± 0.72 mg h^{-1} mg_{cat}^{-1} and a superior FE_{NH3} of 94.8 ± 4.34% at −0.4 V as compared to other electrodes. This observation suggests that the tensile strain and multielemental synergy strategy enhance electrocatalytic activity for NO_3RR.[39] To further assess the practical applicability of the HEA@C-R4 catalyst under diverse wastewater conditions, we expanded the electrochemical evaluation to a broader range of nitrate concentrations (10 mM to 1000 mM). As shown in Figure S27, the catalyst maintained a consistently high FE alongside excellent NH_3 yield rates across a wide concentration range (80−1000 mM). This sustained high performance under varying reactant concentrations confirms the exceptional robustness and practical viability of the HEA@C-R4 catalyst for complex environmental remediation applications. The electrochemically active surface area (ECSA) was also determined to accurately assess the intrinsic activity of these catalysts (Figure S28). As a result, the ECSA normalized current density for NO_3RR ($j_{NH3\text{-}ECSA}$) was shown in Figure 4b, indicating that HEA@C-R4 catalyst had the highest intrinsic activity for NO_3RR across the measured potential range.

To confirm the N source of the produced NH_3, isotope labeling experiments were conducted using ^{15}N-labeled NO_3^- as the reagent. As a result, unlike the three characteristic peaks of $^{14}NH_4^+$, only a doublet peak of $^{15}NH_4^+$ is observed in 1H nuclear magnetic resonance (1H NMR) spectroscopy, confirming that the ammonia formation originated from the $^{15}NO_3^-$ feedstock rather than contamination (Figure S29). Furthermore, when adding $^{14}NO_3^-/^{15}NO_3^-$ in a ratio of 1:1 as the reagent, the ratio of reduction products $^{14}NH_4^+/^{15}NH_4^+$ remains almost unchanged (Figure 4c).[40,41] This result more accurately evidence that ammonia products originate from nitrate's electroreduction.[42] The FE_{NH3} quantified by ^{1}H NMR was very close to the results obtained by ultraviolet−visible

(UV−vis) spectrophotometry, as shown in Figures 4d, S30, and S31, thus confirming the accuracy of the quantitative methods used in this work (Note S3).

The conversion of nitrate to ammonia is a complex process involving an 8-electron transfer, often leading to various byproducts and multiple possible reaction pathways. To investigate the molecular intermediates and products of the HEA@C-R4 material, online differential electrochemical mass spectrometry (DEMS) and density functional theory (DFT) calculations were performed (Figures 4e and S32).[41] Due to space limitations, detailed discussions of the DEMS and DFT results are provided in the SI Appendix (Note S4). Based on the in situ electrochemical analysis and theoretical calculations, the nitrate reduction reaction pathway in this system can be summarized as follows: $NO_3^-\rightarrow$ $*NO_3\rightarrow$ $*NO_2\rightarrow$ $*NO\rightarrow$ $*NOH\rightarrow$ $*NH_2O\rightarrow$ $*NH_2OH\rightarrow$ $*NH_2\rightarrow$ $*NH_3\rightarrow$ NH_3.

To further evaluate the steady state NO_3RR performance of the HEA@C catalysts, chronoamperometry was conducted at a constant potential.[43] As shown in Figure 4f, the chronoamperometric curves of HEA@C-R4 remained nearly unchanged throughout the NO_3RR process, demonstrating excellent operational stability. The Faradaic efficiency for NH_3 also exhibited high durability, with a decrease of less than 10% after 30 consecutive cycles (each cycle lasting 24 h). In contrast, both Cu-NPs and HEA@C-R0 showed a decline in catalytic current after only 3 electrolysis cycles, accompanied by reductions in NH_3 FE of 12 and 11% over 6 and 9 reproducible electrolysis experiments, respectively (Figures S33 and S34). This comparison underscores the superior long-term stability of the multielement nanoparticles. Comparative TEM and statistical size distributions reveal exceptional morphological stability, with the average nanoparticle diameter shifting negligibly after 720 h of continuous electrolysis, completely ruling out severe agglomeration (Figure S35). Furthermore, high-resolution TEM characterizations confirm the preservation of the nanoparticles' microscopic structure, with single-phase FCC crystallinity and well-defined lattice fringes (Figure S36). Further STEM-EDS analysis confirmed the homogeneous distribution of Mn, Fe, Co, Ni, and Cu within the HEA nanoparticles in the HEA@C-R4 sample, with no evidence of phase separation after prolonged operation (Figure S37). Beyond morphological retention, the crystallographic and chemical robustness of the HEA@C catalyst was rigorously verified after 720 h of continuous operation. Postcatalysis XRD (Figure S38) confirmed the complete preservation of the single-phase FCC solid-solution structure without any detectable phase transition, amorphization, or bulk oxide formation. Furthermore, postcatalysis XPS (Figure S39) revealed that the surface chemical states of the constituent transition metals remained virtually identical to those of the pristine catalyst, effectively ruling out any significant surface oxidation during prolonged electrocatalytic NO_3RR. In-situ Raman spectroscopy was employed to monitor potential structural changes in HEA@C-R4. Except for the peaks corresponding to the adsorbed SO_4^{2-} and NO_3^-, no other signals indicative of newly formed phases in HEA are observed in the spectra, affirming the robust structural stability of this multielement alloy (Figure S40). Such excellent, long-term, stable activity clearly outperforms other reported electrocatalytic NO_3^--to-NH_3 conversions (Figure S41 and Tables S9−S11).

2.5. Computational Insights into the NO_3RR on HEA-NPs

To elucidate the mechanism underlying the enhanced activity of HEA catalysts for the nitrate reduction reaction, we conducted first-principles calculations based on structural features, including multielement synergy and inhomogeneous lattice strain. The partial density of states (PDOS) of constituent elements in strained MnFeCoNiCu HEA-NPs was systematically investigated. As illustrated in Figure 5a, pronounced orbital hybridization among most electronic states indicates strong interatomic electronic interactions. This extensive hybridization promotes efficient site-to-site electron transfer during the NO_3RR. In this synergistic mechanism, each element contributes distinct electronic functions: Mn and Fe exhibit highly localized orbitals positioned deep below the Fermi level (E_F), serving as effective electron reservoirs. In contrast, Ni and Co, with their electronic states located near E_F, function as electron-accepting centers that enhance the adsorption of key reaction intermediates. Meanwhile, Cu, characterized by its delocalized, electron-rich orbitals, facilitates rapid electron transfer and enhances bonding to intermediates.[44] This electronic structure configuration collectively enables efficient multielectron transfer processes, enhancing NO_3RR performance.

The distinct electronic roles of constituent elements directly govern their adsorption behaviors toward reaction intermediates. Based on the Bayesian theory of chemisorption, linear scaling relations were identified between the adsorption energies of $*NO_3$ and $*N$ across different metal sites.[45,46] Using the binding strengths of $*NO_3$ and $*N$ as descriptors, we developed an activity volcano plot, where catalytic activity is represented by the maximum free energy barrier along the reaction pathway (Figure 5b). Owing to the diverse active sites in the high-entropy alloy, this volcano relationship provides a predictive tool for estimating the catalytic performance of various active centers. Since bridge-bidentate adsorption is the predominant binding mode, 15 unique coordination environments within the HEA under lattice strain were systematically examined. In monometallic catalyst systems, theoretical analysis reveals intrinsic limitations: sites with overly strong adsorption capabilities decelerate the release of nitrogen-bonded species, thereby increasing the energy barriers of subsequent hydrogenation/dehydration steps; conversely, sites with weak adsorption capabilities result in large energy barriers for NO_3^- capture. Both extremes impede the reaction, consistent with scaling relations for adsorption energy. However, multiple pair-metal sites in the HEA are predicted to be near the top of the activity volcano plot, with appropriate binding energies to balance adsorption and desorption. Among these, the heteronuclear Cu−Fe sites exhibit the highest activity arising from enhanced $*NO_3$ binding and weakened $*N$ adsorption. Electronic structure analysis reveals that the d-band center of Fe atoms in Cu−Fe pairs is shifted upward compared to that of Cu, leading to stronger $*NO_3$ adsorption (Figure 5a). This shift also enhances the hybridization contribution to $*N$ binding, consistent with the conventional d-band model. In contrast, Cu interacts with $*N$ primarily repulsively due to its fully occupied d-band and large d-orbital radius, facilitating the desorption of nitrogen-containing species.[46] Other comparative heteronuclear sites, such as Mn−Fe, Co−Ni, and Mn−Ni pairs, also demonstrate high activities. Furthermore, the multifunctional active centers in the MnFeCoNiCu HEA function as cooperative sites that enable efficient NH_3 electrosynthesis, effectively breaking traditional scaling relationships. For instance, strong-binding sites like Mn−Mn and Fe−Fe readily capture and activate reactants, whereas adjacent weak-binding sites such as Cu−Cu, Ni−Ni, and Cu−Ni facilitate surface refreshing. This multimetal system enables independent tuning of $^*NO_3$ and *N adsorption strengths, thereby optimizing the stabilization and release of key intermediates for efficient electrochemical ammonia synthesis.[47,48] Considering the immense complexity of the local atomic environments in HEAs, specifically, the 13 randomly occupied neighboring atoms within a 3.5 Å radius of the Cu−Fe active site, the dispersion of the adsorption energies in Figure S42 is derived from the statistical calculations of 20 randomly generated distinct coordination configurations (slab structure as shown in Figures S43−45). This dispersion reflects the nonuniformity of the local electronic structures, yet the statistical center confirms that the Cu−Fe sites consistently maintain optimal catalytic activity. Furthermore, to decouple geometric lattice distortion from chemical coordination effects, we compared adsorption energetics with and without the experimentally observed 2.8% surface tensile strain (Figure S46). This lattice expansion effectively shifted the statistical center of the dispersed adsorption energies toward a more optimal binding regime. Calculations on the 2.8% strained active sites reveal a highly negative Gibbs free energy for hydrogen adsorption (Figure S47). This excessively strong H* binding creates a thermodynamic trap that suppresses the competitive HER. To further assess the influence of lattice strain, we compared the predicted activities of strained (2.8% tensile strain) and unstrained HEA models (Figures 5c, S48, and S49). Compared to the unstrained case, the strained surface strengthens $^*NO_3$ adsorption and reduces the thermodynamic barrier for NH_3 release to 0.75 eV, compared to 0.86 eV. These results indicate that introducing lattice strain can enhance NO_3RR catalytic activity, offering a promising strategy for improving electrochemical ammonia synthesis.

3. DISCUSSION

In summary, we have demonstrated that strained HEA-NPs can be synthesized effectively via a nanoconfined alloying strategy, in which Zn serves as an active sacrificial element to form interconnected nanochannels. These channels guide the directional flow of multimetal nanofluids and facilitate the formation of alloys under mild conditions. Notably, in situ TEM observations provided direct evidence of long-range directional nanofluid migration within nanoconfined spaces, which triggers forced fusion and enhanced fission events. These dynamic processes not only promote homogeneous elemental mixing and size-controlled growth but also induce significant surface strain due to the unique nanoconfinement effect during synthesis. This approach enables the incorporation of ten dissimilar metallic elements into uniformly mixed HEA-NPs, offering versatility for a range of functional applications. Particularly in electrocatalytic nitrate-to-ammonia conversion, the synthesized strained quinary HEA-NPs exhibited exceptional performance, achieving a Faradaic efficiency of 94.8 ± 4.34% and maintaining remarkable stability over 720 h, underscoring their practical potential. The origin of such enhanced catalytic performance was systematically investigated through mechanistic studies. It was revealed that the improved activity stems from the synergistic interaction between multielement active sites and the intentionally introduced surface tensile strain, which collectively optimize the adsorption energy of key reaction intermediates. This work introduces an innovative research direction that highlights the critical role of nanoconfinement engineering in facilitating the alloying of immiscible elements and in imparting controlled strain into multimetallic systems. The methodology presented here offers a scalable, generalizable approach for designing compositionally complex HEA-NPs. More broadly, the integration of nanoconfinement and strain engineering opens promising avenues for developing advanced electrocatalysts for a wide spectrum of sustainable energy and catalytic applications.

■ ASSOCIATED CONTENT

Supporting Information

The Supporting Information is available free of charge at https://pubs.acs.org/doi/10.1021/jacs.5c22716.

Detailed experimental procedures, materials and methods, theoretical calculation details, and additional supporting figures and tables (PDF)

In situ TEM videos demonstrating the dynamic alloying process; Zn nanoparticle nucleation (MP4)

Nanofluid propagates through internal nanochannels (MP4)

■ AUTHOR INFORMATION

Corresponding Authors

SenPo Yip − *Institute for Materials Chemistry and Engineering, Kyushu University, Fukuoka 816-8580, Japan;* orcid.org/0000-0002-6622-3982; Email: yip.sen.po.472@m.kyushu-u.ac.jp

Yang Lu − *Department of Mechanical Engineering, The University of Hong Kong, Hong Kong 999077, P. R. China;* orcid.org/0000-0002-9280-2718; Email: ylu1@hku.hk

Johnny C. Ho − *Department of Materials Science and Engineering and State Key Laboratory of Terahertz and Millimeter Waves, City University of Hong Kong, Hong Kong 999077, P. R. China; Institute for Materials Chemistry and Engineering, Kyushu University, Fukuoka 816-8580, Japan;* orcid.org/0000-0003-3000-8794; Email: johnnyho@cityu.edu.hk

Authors

Di Yin − *Department of Materials Science and Engineering, City University of Hong Kong, Hong Kong 999077, P. R. China*

Liqiang Wang − *Department of Mechanical Engineering, City University of Hong Kong, Hong Kong 999077, P. R. China*

You Meng − *Department of Materials Science and Engineering and State Key Laboratory of Terahertz and Millimeter Waves, City University of Hong Kong, Hong Kong 999077, P. R. China;* orcid.org/0000-0002-5385-4080

Mengxue Chen − *Department of Chemistry, City University of Hong Kong, Hong Kong 999077, P. R. China*

Dong Chen − *Department of Materials Science and Engineering, City University of Hong Kong, Hong Kong 999077, P. R. China*

Chenxu Zhang − *Department of Materials Science and Engineering, City University of Hong Kong, Hong Kong 999077, P. R. China; State Key Laboratory of Radio Frequency Heterogeneous Integration (Shenzhen University), College of Electronics and Information Engineering, Shenzhen 518060, P.R. China*

Quan Quan − *Department of Materials Science and Engineering, City University of Hong Kong, Hong Kong 999077, P. R. China*
Haifan Li − *Department of Chemistry, City University of Hong Kong, Hong Kong 999077, P. R. China*
Liyuan Dai − *Interdisciplinary Graduate School of Engineering Sciences, Kyushu University, Fukuoka 816-8580, Japan*
Lijie Chen − *CIMC Offshore Co., Ltd., Shenzhen 518000, P.R. China*
Cheng Yang − *Institute of Materials Research, Tsinghua Shenzhen International Graduate School, Tsinghua University, Shenzhen 518055, P. R. China;* orcid.org/0000-0003-2618-4787
Chun-Yuen Wong − *Department of Chemistry, City University of Hong Kong, Hong Kong 999077, P. R. China;* orcid.org/0000-0003-4780-480X
Takeshi Yanagida − *Institute for Materials Chemistry and Engineering, Kyushu University, Fukuoka 816-8580, Japan; Department of Applied Chemistry, Graduate School of Engineering, The University of Tokyo, Tokyo 113-8656, Japan;* orcid.org/0000-0003-4837-5701

Complete contact information is available at: https://pubs.acs.org/10.1021/jacs.5c22716

Author Contributions

●D.Y. and L.W. are contributed equally.

Notes

The authors declare no competing financial interest.

■ ACKNOWLEDGMENTS

This work was financially supported by the City University of Hong Kong (Project Nos. 9229138, 9231502, and 9231539, J.C.H.), the Hong Kong RGC general research fund (Project No. 11200623, T45-406/23-R, Y.L.), the Science Technology and Innovation Committee of Shenzhen Municipality (Project No. JCYJ20230807114910021, J.C.H.), the Guangdong Provincial Science and Technology Plan Project (No. 2025A0505080006, J.C.H.), and the Guangdong Provincial Basic and Applied Basic Research Project (No. 2024B1515120005, J.C.H.).

■ REFERENCES

(1) Sun, Y.; Dai, S. High-entropy materials for catalysis: A new frontier. *Sci. Adv.* **2021**, *7* (20), No. eabg1600.

(2) Ma, Y.; Ma, Y.; Wang, Q.; Schweidler, S.; Botros, M.; Fu, T.; Hahn, H.; Brezesinski, T.; Breitung, B. High-entropy energy materials: challenges and new opportunities. *Energy Environ. Sci.* **2021**, *14* (5), 2883−2905.

(3) Zhan, C.; Bu, L.; Sun, H.; Huang, X.; Zhu, Z.; Yang, T.; Ma, H.; Li, L.; Wang, Y.; Geng, H.; et al. Medium/High-Entropy Amalgamated Core/Shell Nanoplate Achieves Efficient Formic Acid Catalysis for Direct Formic Acid Fuel Cell. *Angew. Chem., Int. Ed.* **2023**, *62* (3), No. e202213783.

(4) Wei, Y.; Yao, R.; Liu, X.; Chen, W.; Qian, J.; Yin, Y.; Li, D.; Chen, Y. Understanding the configurational entropy evolution in metal-phosphorus solid solution for highly reversible Li-ion batteries. *Adv. Sci.* **2023**, *10* (9), No. 2300271.

(5) Chen, Z. W.; Li, J.; Ou, P.; Huang, J. E.; Wen, Z.; Chen, L.; Yao, X.; Cai, G.; Yang, C. C.; Singh, C. V.; et al. Unusual Sabatier principle on high entropy alloy catalysts for hydrogen evolution reactions. *Nat. Commun.* **2024**, *15* (1), 359.

(6) Sun, X.; Sun, Y. Synthesis of metallic high-entropy alloy nanoparticles. *Chem. Soc. Rev.* **2024**, *53* (9), 4400−4433.

(7) Wang, B.; Wang, C.; Yu, X.; Cao, Y.; Gao, L.; Wu, C.; Yao, Y.; Lin, Z.; Zou, Z. General synthesis of high-entropy alloy and ceramic nanoparticles in nanoseconds. *Nat. Synth.* **2022**, *1* (2), 138−146.

(8) Cao, G.; Liang, J.; Guo, Z.; Yang, K.; Wang, G.; Wang, H.; Wan, X.; Li, Z.; Bai, Y.; Zhang, Y.; et al. Liquid metal for high-entropy alloy nanoparticles synthesis. *Nature* **2023**, *619* (7968), 73−77.

(9) Yao, Y.; Huang, Z.; Xie, P.; Lacey, S. D.; Jacob, R. J.; Xie, H.; Chen, F.; Nie, A.; Pu, T.; Rehwoldt, M.; et al. Carbothermal shock synthesis of high-entropy-alloy nanoparticles. *Science* **2018**, *359* (6383), 1489−1494.

(10) Qiao, H.; Saray, M. T.; Wang, X.; Xu, S.; Chen, G.; Huang, Z.; Chen, C.; Zhong, G.; Dong, Q.; Hong, M.; et al. Scalable synthesis of high entropy alloy nanoparticles by microwave heating. *ACS Nano* **2021**, *15* (9), 14928−14937.

(11) Tammann, G.; Mansuri, Q. Metallographische mitteilungen aus dem Institut für physikalische chemie der universität göttingen CXIII. Zur Rekristallisation von Metallen und Salzen. *Zeitschrift für anorganische und allgemeine Chemie* **1923**, *126* (1), 119−128.

(12) Gao, S.; Hao, S.; Huang, Z.; Yuan, Y.; Han, S.; Lei, L.; Zhang, X.; Shahbazian-Yassar, R.; Lu, J. Synthesis of high-entropy alloy nanoparticles on supports by the fast moving bed pyrolysis. *Nat. Commun.* **2020**, *11* (1), 2016.

(13) Feng, J.; Chen, D.; Pikhitsa, P. V.; Jung, Y.-h.; Yang, J.; Choi, M. Unconventional alloys confined in nanoparticles: building blocks for new matter. *Matter* **2020**, *3* (5), 1646−1663.

(14) Waag, F.; Li, Y.; Ziefuß, A. R.; Bertin, E.; Kamp, M.; Duppel, V.; Marzun, G.; Kienle, L.; Barcikowski, S.; Gökce, B. Kinetically-controlled laser-synthesis of colloidal high-entropy alloy nanoparticles. *RSC Adv.* **2019**, *9* (32), 18547−18558.

(15) Buffat, P.; Borel, J. P. Size effect on the melting temperature of gold particles. *Phys. Rev. A* **1976**, *13* (6), 2287.

(16) Saidur, R.; Leong, K.; Mohammed, H. A. A review on applications and challenges of nanofluids. *Renewable Sustainable Energy Rev.* **2011**, *15* (3), 1646−1668.

(17) Kalantar-Zadeh, K.; Tang, J.; Daeneke, T.; O'Mullane, A. P.; Stewart, L. A.; Liu, J.; Majidi, C.; Ruoff, R. S.; Weiss, P. S.; Dickey, M. D. Emergence of liquid metals in nanotechnology. *ACS Nano* **2019**, *13* (7), 7388−7395.

(18) Hao, J.; Zhuang, Z.; Cao, K.; Gao, G.; Wang, C.; Lai, F.; Lu, S.; Ma, P.; Dong, W.; Liu, T.; et al. Unraveling the electronegativity-dominated intermediate adsorption on high-entropy alloy electrocatalysts. *Nat. Commun.* **2022**, *13* (1), 2662.

(19) Zhu, H.; Sun, S.; Hao, J.; Zhuang, Z.; Zhang, S.; Wang, T.; Kang, Q.; Lu, S.; Wang, X.; Lai, F.; et al. A high-entropy atomic environment converts inactive to active sites for electrocatalysis. *Energy Environ. Sci.* **2023**, *16* (2), 619−628.

(20) Fan, L.; Ji, Y.; Wang, G.; Chen, J.; Chen, K.; Liu, X.; Wen, Z. High entropy alloy electrocatalytic electrode toward alkaline glycerol valorization coupling with acidic hydrogen production. *J. Am. Chem. Soc.* **2022**, *144* (16), 7224−7235.

(21) Cai, R.; Guo, S.; Meng, Q.; Yang, S.; Xin, H. L.; Hu, X.; Li, M.; Sun, Y.; Gao, P.; Zhang, S.; et al. Atomic-level tunnel engineering of todorokite MnO2 for precise evaluation of lithium storage mechanisms by in situ transmission electron microscopy. *Nano Energy* **2019**, *63*, 103840.

(22) Lu, Y.; Huang, J. Y.; Wang, C.; Sun, S.; Lou, J. Cold welding of ultrathin gold nanowires. *Nat. Nanotechnol.* **2010**, *5* (3), 218−224.

(23) Zhao, R.; Liang, Z.; Gao, S.; Yang, C.; Zhu, B.; Zhao, J.; Qu, C.; Zou, R.; Xu, Q. Puffing up energetic metal−organic frameworks to large carbon networks with hierarchical porosity and atomically dispersed metal sites. *Angew. Chem., Int. Ed.* **2019**, *58* (7), 1975−1979.

(24) Yin, S.; Yi, H.; Liu, M.; Yang, J.; Yang, S.; Zhang, B.-W.; Chen, L.; Cheng, X.; Huang, H.; Huang, R.; et al. An in situ exploration of how Fe/N/C oxygen reduction catalysts evolve during synthesis under pyrolytic conditions. *Nat. Commun.* **2024**, *15* (1), 6229.

(25) Li, C.; Zhang, Z.; Zhu, K.; Liu, M.; Chen, J.; Zhou, L.; Zhang, Q.; Wu, Y.; Guo, J.; Shi, R.; et al. Nanoconfined impulse synthesis of

high-entropy nanocarbides for active and stable electrocatalysis. *Nat. Synth.* **2025**, *4* (11), 1422−1434.

(26) Anbarasu, M.; Gurusamy, A.; Saravanan, S. Properties of different graded coir pith by Keen-Raczkowski box and Brunauer-Emmett-Teller analysis. *J. Environ. Biol.* **2024**, *45* (3), 357−362.

(27) Yang, L.; He, R.; Chai, J.; Qi, X.; Xue, Q.; Bi, X.; Yu, J.; Sun, Z.; Xia, L.; Wang, K.; et al. Synthesis strategies for high entropy nanoparticles. *Adv. Mater.* **2025**, *37* (1), No. 2412337.

(28) Meng, Z.; Xu, Z.; Tian, H.; Zheng, W. Insights into high-entropy material synthesis dynamics criteria based on a thermodynamic framework. *Mater. Horiz.* **2023**, *10* (9), 3293−3303.

(29) Paul, A.; Laurila, T.; Vuorinen, V.; Divinski, S. V.; Paul, A.; Laurila, T.; Vuorinen, V.; Divinski, S. V., Fick's laws of diffusion. In *Thermodynamics, diffusion and the kirkendall effect in solids*, 2014; pp 115−139.

(30) Li, X.; Zhou, Y.; Feng, C.; Wei, R.; Hao, X.; Tang, K.; Guan, G. High entropy materials based electrocatalysts for water splitting: Synthesis strategies, catalytic mechanisms, and prospects. *Nano Res.* **2023**, *16* (4), 4411−4437.

(31) Yang, H.; Drossinos, Y.; Hogan, C. J. Excess thermal energy and latent heat in nanocluster collisional growth. *J. Chem. Phys.* **2019**, *151* (22), 224304.

(32) Guo, K.; Bao, L.; Yu, Z.; Xing, L. Carbon encapsulated nanoparticles: materials science and energy applications. *Chem. Soc. Rev.* **2024**, *53*, 1.

(33) Gu, J.; Duan, F.; Liu, S.; Cha, W.; Lu, J. Phase engineering of nanostructural metallic materials: classification, structures, and applications. *Chem. Rev.* **2024**, *124* (3), 1247−1287.

(34) Gao, Q.; Yao, B.; Pillai, H. S.; Zang, W.; Han, X.; Liu, Y.; Yu, S.-W.; Yan, Z.; Min, B.; Zhang, S.; et al. Synthesis of core/shell nanocrystals with ordered intermetallic single-atom alloy layers for nitrate electroreduction to ammonia. *Nat. Synth.* **2023**, *2* (7), 624−634.

(35) Sun, Y.; Dai, S. Synthesis of high-entropy materials. *Nat. Synth.* **2024**, *3*, 1457−1470.

(36) Wang, Y.; Wang, C.; Li, M.; Yu, Y.; Zhang, B. Nitrate electroreduction: mechanism insight, in situ characterization, performance evaluation, and challenges. *Chem. Soc. Rev.* **2021**, *50* (12), 6720−6733.

(37) van Langevelde, P. H.; Katsounaros, I.; Koper, M. T. Electrocatalytic nitrate reduction for sustainable ammonia production. *Joule* **2021**, *5* (2), 290−294.

(38) Zhang, H.; Wang, H.; Cao, X.; Chen, M.; Liu, Y.; Zhou, Y.; Huang, M.; Xia, L.; Wang, Y.; Li, T.; et al. Unveiling cutting-edge developments in electrocatalytic nitrate-to-ammonia conversion. *Adv. Mater.* **2024**, *36* (16), No. 2312746.

(39) Chen, D.; Yin, D.; Zhang, S.; Yip, S.; Ho, J. C. Nitrate electroreduction: recent development in mechanistic understanding and electrocatalyst design. *Mater. Today Energy* **2024**, *44*, No. 101610.

(40) Wang, Y.; Xu, A.; Wang, Z.; Huang, L.; Li, J.; Li, F.; Wicks, J.; Luo, M.; Nam, D.-H.; Tan, C.-S.; et al. Enhanced nitrate-to-ammonia activity on copper−nickel alloys via tuning of intermediate adsorption. *J. Am. Chem. Soc.* **2020**, *142* (12), 5702−5708.

(41) Ni, J.; Yan, J.; Li, F.; Qi, H.; Xu, Q.; Su, C.; Sun, L.; Sun, H.; Ding, J.; Liu, B. Atomic Co— P Catalytic Pair Drives Efficient Electrochemical Nitrate Reduction to Ammonia. *Adv. Energy Mater.* **2024**, *14* (28), No. 2400065.

(42) Chen, D.; Zhang, S.; Bu, X.; Zhang, R.; Quan, Q.; Lai, Z.; Wang, W.; Meng, Y.; Yin, D.; Yip, S.; et al. Synergistic modulation of local environment for electrochemical nitrate reduction via asymmetric vacancies and adjacent ion clusters. *Nano Energy* **2022**, *98*, No. 107338.

(43) Yao, Y.; Liu, Z.; Xie, P.; Huang, Z.; Li, T.; Morris, D.; Finfrock, Z.; Zhou, J.; Jiao, M.; Gao, J. Computationally aided, entropy-driven synthesis of highly efficient and durable multi-elemental alloy catalysts. *Sci. Adv.* **2020**, *6* (11), No. eaaz0510.

(44) Zhou, Y.; Zhang, L.; Wang, M.; Shen, X.; Zhu, Z.; Qian, T.; Yan, C.; Lu, J. Maximized atom utilization in a high-entropy metallene via single atom alloying for boosted nitrate electroreduction to ammonia. *Nat. Commun.* **2025**, *16* (1), 7915.

(45) Niu, H.; Zhang, Z.; Wang, X.; Wan, X.; Shao, C.; Guo, Y. Theoretical insights into the mechanism of selective nitrate-to-ammonia electroreduction on single-atom catalysts. *Adv. Funct. Mater.* **2021**, *31* (1), No. 2008533.

(46) Wang, S.; Pillai, H. S.; Xin, H. Bayesian learning of chemisorption for bridging the complexity of electronic descriptors. *Nat. Commun.* **2020**, *11* (1), 6132.

(47) Zhu, J.; Xiao, M.; Ren, D.; Gao, R.; Liu, X.; Zhang, Z.; Luo, D.; Xing, W.; Su, D.; Yu, A.; et al. Quasi-covalently coupled Ni−Cu atomic pair for synergistic electroreduction of CO_2. *J. Am. Chem. Soc.* **2022**, *144* (22), 9661−9671.

(48) Gao, Q.; Pillai, H. S.; Huang, Y.; Liu, S.; Mu, Q.; Han, X.; Yan, Z.; Zhou, H.; He, Q.; Xin, H.; et al. Breaking adsorption-energy scaling limitations of electrocatalytic nitrate reduction on intermetallic CuPd nanocubes by machine-learned insights. *Nat. Commun.* **2022**, *13* (1), 2338.